Available online at www.sciencedirect.com
ScienceDirect
C. R. Physique 9 (2008) 248–261
COMPTES RENDUS PHYSIQUE
http://france.elsevier.com/direct/COMREN/

Recent developments in terahertz optoelectronics/Développements récents en optoélectronique térahertz

# Detection of explosives by Terahertz synthetic aperture imaging—focusing and spectral classification

Alexander Sinyukov [a], Ivan Zorych [b], Zoi-Heleni Michalopoulou [b], Dale Gary [a], Robert Barat [c], John F. Federici [a,*]

[a] *Department of Physics, New Jersey Institute of Technology, Newark, NJ, USA*
[b] *Department of Mathematical Sciences, New Jersey Institute of Technology, Newark, NJ, USA*
[c] *Otto York Department of Chemical Engineering, New Jersey Institute of Technology, Newark, NJ, USA*

Available online 9 January 2008

**Abstract**

In the adaptation of Terahertz (THz) synthetic aperture imaging to stand-off screening of concealed weapons and explosives, the incoming THz wavefronts exhibit significant curvature that must be considered in the image reconstruction. Consequently, the imaging array must be focused at a specific distance to correct for the wavefront curvature. In addition to the focusing correction, detection of explosives requires spectral analysis of the reconstructed THz image. Kohonen self-organizing maps are shown to be promising tools for differentiating the spectral signature of C4 explosive from the reflection spectra of metal and semi-transparent barrier materials. ***To cite this article: A. Sinyukov et al., C. R. Physique 9 (2008).***


**Résumé**

**Détection d'explosives par l'imagerie térahertz à ouverture synthétique : mise au point et classification spectrale.** Nous nous intéressons ici à la détection d'armes et de substances explosives par l'imagerie térahertz à ouverture synthétique. Dans cette technique, le front d'onde THz réfléchi par l'objet observé présente une déformation importante qui doit être prise en compte dans la reconstruction de l'image. Il en découle que le détecteur matriciel doit être situé à une distance spécifique pour corriger l'effet de cette déformation. En plus de la correction du front d'onde, la détection d'explosifs demande une analyse spectrale de l'image. Nous montrons, en prenant comme exemple l'explosif C4, que la méthode de cartographie auto-organisée de Kohonen constitue un outil efficace pour différencier la signature spectrale des explosifs de celle de l'environnement. ***Pour citer cet article : A. Sinyukov et al., C. R. Physique 9 (2008).***


*Keywords:* Terahertz; Kohonen maps; Synthetic aperture

*Mots-clés :* Térahertz ; Cartographie de Kohonen ; Ouverture synthétique

* Corresponding author.
*E-mail addresses:* sinyukov@njit.edu (A. Sinyukov), zorych@njit.edu (I. Zorych), michalop@njit.edu (Z.-H. Michalopoulou), dgary@njit.edu (D. Gary), barat@adm.njit.edu (R. Barat), federici@adm.njit.edu (J.F. Federici).

1631-0705/$ – see front matter 
doi:10.1016/j.crhy.2007.09.013

## 1. Introduction

Over the past several years, there has been an increased interest in the potential of Terahertz (THz) detection for imaging of concealed weapons, explosives, chemical and biological agents [1,2]. There are three major factors contributing to this interest:

- Terahertz radiation is readily transmitted through most non-metallic and non-polar mediums, thus enabling THz systems to 'see through' concealing barriers such as packaging, corrugated cardboard, clothing, shoes, book bags, etc. in order to probe the potentially dangerous materials contained within.
- Many materials of interest for security applications, including explosives, chemical agents, and biological agents, have characteristic THz spectra that can be used to fingerprint and thereby identify these concealed materials.
- Terahertz radiation poses either no or minimal health risk to either a suspect being scanned by a THz system or the system's operator.

As plastic explosives, fertilizer bombs, chemical and biological agents increasingly become weapons of war and terrorism, effective means for rapid detection and identification of these threats are required. One proposed solution for locating, detecting and characterizing concealed threats is to use THz electromagnetic waves to spectroscopically detect and identify concealed materials through their characteristic transmission or reflectivity spectra in the range of 0.5–10 THz. For example, many explosives (for example C-4, HMX, RDX, TNT) have characteristic transmission/reflection spectra in the THz range that could be distinguishable from other materials such as clothing, coins, and human skin. In essence, these materials should appear as different colors to the THz detector as compared to non-hazardous items. Using THz spectroscopy it should be possible to detect explosives even if they are concealed since the THz radiation is readily transmitted through plastics, clothing, luggage, paper products, and other non-conductive (non-metallic) materials. By comparing measured reflectivity THz spectra with known calibration spectra, one may identify the presence of these agents and distinguish them from benign objects.

One complication with imaging at different THz frequencies is that the overall spatial resolution of the THz imaging depends on the wavelength of the lowest THz frequency. This is essentially a diffraction effect: the larger THz wavelengths cannot spatially resolve as small an object as the smaller wavelengths. Consequently, when THz images are analyzed for the spectral presence of an explosive, the edges or boundaries of the explosive might be subject to uncertainty.

In this article, we focus on two topics. The first emphasizes the focusing of the THz interferometric imaging array on targets at various distances. This focusing is required due to the curvature of the THz wavefronts that are reflected from target objects. In the second topic, we explore the use of Kohonen self-organizing maps to classify the spectral images. In Section 2, the interaction of THz radiation with explosives and other materials is discussed. In Section 3, various methods of THz imaging are briefly reviewed. Section 4 develops the theory of THz interferometric imaging. Experimentally measured THz images are discussed in Section 5, while Section 6 discusses the implementation of Artificial Neural Networks and Kohonen Maps to spectrally classify the THz images.

## 2. Interaction of Terahertz radiation with explosives

The ability of THz light to interact differently with benign and threat materials as a function of THz frequency yields a highly flexible foundation for THz imaging security screening based on spectroscopy. In general, non-polar, non-metallic solids such as plastics and ceramics are at least partially transparent and reflective in the 0.2 to 5 THz range. Non-polar liquids are transparent as well, whereas polar liquids, such as water, are highly absorptive: Absorption in the THz range of the electromagnetic spectrum is generally due to interaction of the electromagnetic wave with a dipole moment. Crystals formed from polar liquids are substantially more transparent because the dipolar rotations have been frozen out. However these crystals may exhibit phonon resonances in the THz range.

The vibrations within a molecular crystal cell are not only a result of molecular motions, but also the relative motions between neighboring molecules. Dominant features of the THz spectra are the sharp absorption peaks caused by phonon modes directly related to the crystalline structure [1]. This result originates from the molecular vibrational modes and intramolecular vibrations associated, for example, with RDX [3]. Consequently, vibrational modes are unique and distinctive feature of the crystalline explosive materials. Since many of the crystalline explosives typically

have low vapor pressure, THz spectroscopy offers a potentially useful detection method alternative to those techniques that require a relatively high vapor pressure. The presence of broad features might also be caused by scattering from a structure with dimensions comparable to the THz wavelength. This can occur in materials that contain fibers or grains.

Typical clothing items and paper and plastic packaging should appear transparent in the THz regime. Metals completely block or reflect THz waves. Ceramic guns and knives would partially reflect the THz light. Images of concealed objects such as concealed metallic or plastic knives are sharp and can be identified when imaged with THz [4]. Skin, because of its high water content, would absorb or reflect nearly all T-rays. Consequently, detection of concealed explosives on a person by necessity must be done in a reflection mode. In this scenario, a bright THz source illuminates the person under study, for example. The THz radiation propagates through the clothing, reflects from the hidden explosive, propagates back through the clothing and is finally detected. Both close proximity ($<3$ m) and stand-off detection ($>3$ m) of concealed threat materials requires consideration of THz transmission through barrier materials.

Under realistic circumstances, a target threat material will be concealed in a package, under clothing, etc. Such barrier materials that conceal the threat material have their own characteristic THz transmission spectra that must be taken into account. For example, a barrier material might absorb THz radiation and therefore limit the maximum thickness of material that the THz can 'see through'. It is also possible that the barrier material could exhibit similar THz absorption peaks that could mask the spectral characteristics of the explosives. However, most barrier materials such as cloth, paper, and plastic show a THz absorption spectra that is gradually increasing with frequency, particularly below 3 THz.

A standoff THz detection system must be capable of propagating short (3–100 m) distances through the atmosphere. Atmospheric absorption occurs at specific frequencies. However, there are numerous transmission bands throughout the THz frequency range [5]. While the THz attenuation in the transmission bands is frequency dependent, a typical number is 50 dB/km at 0.8 THz. A stand-off sensing system should be tuned to these transmission bands (e.g. centered at 0.5, 0.65, 0.87, 1.02, 1.29, 1.36, and 1.52 THz) to minimize the absorptive losses of THz radiation by the atmosphere. While atmosphere attenuation is predominately due to absorption of the THz radiation by water vapor, other attenuation effects such as dust, smoke, fog, and rain could effect the THz transmission. It is thought that rain would increase the effective attenuation due to increased water absorption, while typical micron-scale particles such as dust, pollens, and smoke, would not greatly scatter the THz radiation [6], since the THz wavelength is much longer than typical micron-scale particles.

## 3. Terahertz imaging techniques

THz imaging has been rapidly evolving due to advances in THz sources, detectors, and device fabrication methods. A high speed THz imaging device that can scan and positively identify harmful materials at a rapid (video) frame rate is in high demand for security applications. THz images typically have diffraction limited spatial resolution in the $\sim$1 mm range. For security screening applications, this is sufficient resolution to resolve the shapes of guns, knives and other concealed weapons with comparable resolution to simple visible video images [7].

There are three modes of THz imaging. The simplest is a single transmitter and detector; i.e., line-of-sight detection. An image is obtained on a point-by-point basis by scanning the transmitter/detector pair over the sample under test and recording the THz phase and amplitude at each point. Using this method, THz images of macroscopic objects have been obtained. A logical extension of the point detection system is to replace a single detector with a detector array to produce a THz 'digital camera'. However, the technological realization of such an instrument remains elusive. Consequently, one needs to employ alternate scanning methods to increase the imaging speed and pixel count of images.

An alternative THz imaging method is to up-shift the THz spatial (and spectral) information to an alternative electromagnetic frequency range for which image acquisition is more easily implemented. For example, in the electro-optic THz imaging method [8], THz images are shifted into the visible range where conventional CCD cameras acquire images at a very rapid rate.

A third class of THz imaging has emerged over the past few years. Borrowed relatively recently from their extensive use in astronomy and radar ranging [9], THz synthetic aperture imaging uses the measured THz phase and amplitude from multiple positions or from multiple beam paths to reconstruct a THz image. Examples of synthetic aperture imaging using multiple detector positions include THz impulse imaging [10], which shares many features with optical

holography. By measuring the phase and amplitude of the scattered THz radiation as a function of scattering angle and rotation of the target, the geometrical shape of the target can be reconstructed.

Other methods of image reconstruction use a wave propagation equation to back-propagate the scattered radiation to reconstruct the scattering object [11,12]. Examples utilizing arrayed optical mirrors include synthetic phased array THz imaging [13], to reconstruct field amplitude or energy density, diffraction-limited, THz images. Using this method, many individual images can be recorded and superimposed to produce a higher resolution image.

The main subject of this paper, synthetic aperture image reconstruction using the interferometric imaging method, detects the THz electric field at multiple locations. By correlating the phase and amplitude of the electric field from select pairs of detectors, an image can be reconstructed with a relatively few number of detectors [9].

## 4. Interferometric imaging with Terahertz

Interferometric imaging has been suggested as a novel imaging modality for standoff detection of explosives, weapons, and other threats [1,2]. To apply the interferometric synthetic aperture imaging method to the THz range, the basic techniques of radio interferometry [9] are employed. Signals at two or more points in space (i.e. the aperture plane at which the detectors are located) are brought together with the proper delay, and correlated both in phase and quadrature to produce cosine and sine components of the brightness distribution. This technique thus measures both amplitude and phase of the incoming signals. If measured from a sufficient number of points in the aperture plane, the original brightness distribution can be synthesized (imaged) through standard Fourier inversion.

Theoretically, the THz interferometric imaging array approach should have sufficient spatial resolution to detect centimeter-sized concealed explosives from standoff distances [1,2]. A longer-term advantage is that interferometric imaging may produce more information than a single line-of-sight system. With repeated measurements, it should be possible to apply image processing/computational techniques to multiple images and THz sources to aid in noise and false alarm reduction. The tradeoff with the interferometric imaging method is to reduce the number elements in the detector array at the expense of increased complexity in post-detection image reconstruction. In particular, the measured electric fields from each pair of detectors must be correlated in time.

### *4.1. Theory*

The imaging interferometer consists of an array of individual detectors or sensors. Each pair of THz detectors measures the amplitude and phase of incoming THz radiation. As a wave-front of THz radiation encounters the array, each pair of detectors measures one spatial Fourier component of the incoming THz radiation as determined by the separation (baseline) of the detector pair. Each spatial Fourier component is represented as a point in the Fourier transform ($u$–$v$) plane. In order to image the source, additional measurements from other baselines must be included. Since every baseline determines a singe spatial frequency, it is best to have a zero-redundant (i.e. non-periodic) detector array. For a given number of detectors $N$, there are $N(N-1)/2$ possible baseline combinations. The quality of an image depends on the coverage of the $u$–$v$ plane; i.e., the number of different points generated in the $u$–$v$ plane. This in turn depends on the arrangement of the detecting elements of the imaging interferometer array. The primary concern in designing the configuration of detectors is to obtain an efficient coverage of the $u$–$v$ plane over a range determined by the required angular resolution.

For interferometric detection, the correlation of the electric fields at the various pairs of detectors is calculated. It can be shown that the mutual coherence function of the electric fields from detectors placed at positions 1 and 2 can be written as [9]

$$C_{1,2} = \int_S \frac{\sigma_E(\mathbf{r}')\exp(\mathrm{i}k(\mathbf{r}_1 - \mathbf{r}_2))}{r_1 r_2}\,\mathrm{d}S' \tag{1}$$

where $\sigma_E(\mathbf{r}')$ is the time-averaged intensity of the surface at $\mathrm{d}S'$, and the integral is over the surface $S$ of the radiating source (see Fig. 1). Assuming that $|\mathbf{r}' - \mathbf{r}|/Z_o \ll 1$, $r_1 - r_2$ becomes

$$r_1 - r_2 = \frac{x_1^2 - x_2^2 + y_1^2 - y_2^2}{2Z_o} + \frac{(x_2 - x_1)x' + (y_x - y_x)y'}{Z_o} \tag{2}$$

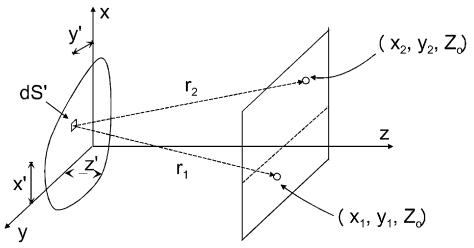


Fig. 1. Source $\mathrm{d}S'$ on surface of $z = z'$ plane irradiating a pair of detectors on the imaging array plane located at $(x_1, y_1, Z_o)$ and $(x_2, y_1, Z_o)$.

where $Z_o$ is the distance along the $z$ axis between the object and imaging array, and $x'$, $y'$, $z'$ locate the spatial coordinates of the object. Using the following definitions, $u = k(x_1 = x_2)/2\pi$, $v = k(y_1 - y_2)/2\pi$, $\xi = x'/Z_o$ and $\eta = y'/Z_o$, the coherence function of Eq. (1) can be cast into the form [9]

$$C_{1,2}(u, v) = \exp(\mathrm{i}\delta) \int_{-\infty}^{\infty} \int_{-\infty}^{\infty} \sigma_E(\xi, \eta) \exp\bigl(-\mathrm{i}2\pi(u\xi + v\eta)\bigr)\, \mathrm{d}\xi\, \mathrm{d}\eta \tag{3}$$

where the denominator of Eq. (3) has been approximated as $1/r_1 r_2 \approx 1/Z_o^2$. If an object is in the far-field ($\delta \ll 1$), the phase shift $\delta = k(x_1^2 - x_2^2 + y_1^2 - y_2^2)/2Z_o$ can be neglected and Eq. (3) will relate the coherence function in the antenna plane to the brightness distribution of the source(s). By a Fourier transform, the brightness distribution (image) can be reconstructed by measuring the coherence function for a given arrangement of detectors in the sensor array. Imaging with a significant phase shift results in a blurred image quality.

### *4.2. Near-field versus far-field*

With radio wave interferometric imaging of astronomical sources, it is typically assumed that the incoming radiation consists of planar waves. In this limit, any curvature of the incoming wavefronts is negligible. This far-field assumption is used for synthetic imaging and simplifies the imaging reconstruction process. However, most standoff THz applications do not fall in the 'far-field' limit [1], and the simplified inverse Fourier transform of the electric field correlation—the far-field image reconstruction—must be modified [14] to account for the curvature of the wave fronts in the near-field.

The blurring of the THz image for stand-off applications can be greatly reduced by altering the arrangement of the detectors in the imaging array. In essence, the arrangement of the detectors in the array must be modified to focus the imaging array at stand-off distances. In one such method, the curvature of the imaging array is matched to that of the wavefront. We assume that two individual detectors of the spherical imaging array measure an electric field from an element of surface $\mathrm{d}S$. For simplicity, we assume that the detectors lay on a spherical surface whose radius of curvature $R_o$ is centered on the origin. The correlation between the two wavefronts at the two detectors can be calculated from Eq. (1) with the detector locations expressed in spherical coordinates $(r, \theta, \phi)$. One can show [1] that the coherence function becomes Eq. (3) with the phase error now given by $\bar{\delta} = kz'(\cos\theta_2 - \cos\theta_1)$. If the near-field phase error can be neglected, Eq. (3) would then relate the coherence function to the brightness distribution of the source. It can be shown that one consequence of the focusing of the near-field array is a restriction on the depth of focus for a fixed configuration of the detector array.

Ignoring any near-field correction, the THz line image is reconstructed [1,27] from Eq. (3) using the following formulas

$$\sigma_E(\xi, \eta) = \sum_{l=1}^{N(N-1)/2} \bigl[Re(C_l)\cos\bigl(k(u_l\xi + v_l\eta)\bigr) - Im(C_l)\sin\bigl(k(u_l\xi + v_l\eta)\bigr)\bigr] \tag{4}$$

$$u_l = \frac{(x_n - x_m)}{\lambda}, \qquad v_l = \frac{(y_n - y_m)}{\lambda} \tag{5}$$

where $\sigma_E$ is the brightness distribution (image), $\xi = x/Z_o$ and $\eta = y/Z_o$, $x_n$, $x_m$ and $y_n$, $y_m$ are the detector positions along $x$- and $y$-axis respectively, and the iteration of $n$ and $m$ is chosen such that each baseline combination (from the $N(N-1)/2$ possible) is included. $C_l$ is the correlation function given by

$$C_l = A_l \exp(\mathrm{i}k\Delta\phi_l) \tag{6}$$

where $A_l = E_m E_n$ and $\Delta\phi = \phi_m - \phi_n$ represent the product of the electric field amplitudes and change in phase for each baseline pair combination. Corrections to the near-field may be introduced by adjusting the measured phases. The summation over $l$ includes in the reconstructed image the contribution from each spatial Fourier component corresponding to each unique baseline separation. The above equations represent the simplest reconstruction of the image: the correlation function for each possible unmeasured baseline pair combination is assumed to be zero.

For the near-field correction, the appropriate phase is added to the measured THz phase such that the position of the detectors is moved to 'deform' the locations of the detectors from a plane to a curved surface whose radius of curvature matches the curvature of the incoming waveforms. Consequently, the measured phase of the THz waves at each detector position can be corrected according to the formula,

$$\phi_{\mathrm{corr}} = \phi_{\mathrm{meas}} - k\left(\sqrt{x_l^2 + y_l^2 + Z_o^2} - Z_o\right) \tag{7}$$

where $k$ is the wave number, $x_l$ and $y_l$ are the coordinates of the detector, $Z_o$ is the distance between the target and the detector array plane along the $z$-axis.

## 5. Experimental Terahertz imaging

### 5.1. Terahertz photo-mixing system

To experimentally demonstrate THz image reconstruction and focusing using interferometric imaging, a continuous wave (CW) THz generation and detection method is employed. In particular, infrared light from two External Cavity Diode Lasers (ECDL) in the Littrow configuration are mixed in a photoconductive antenna structure. Details of the experimental system may be found in Ref. [14].

In absence of the availability of multiple THz detectors for a complete $N$ element detector array, we use a single THz detector at multiple positions to sample the phase and amplitude of the wavefront from a point-like THz source. The electric field correlation can then be calculated for each pair of detector positions, thereby mimicking the performance of an $N$ element detector array. The relative reference phase for each 'detector' remains fixed since the infrared signals are delivered to the receiver via a fixed-length fiber-pigtail.

In Fig. 2, the spiral detector array of 64 detector positions shown were used for our two-dimensional imaging. At every detector location, the corresponding amplitude and phase of THz field is recorded. Two computer controlled translation stages move the receiver laterally to different locations corresponding to different 'detectors' in the interferometric imaging array.

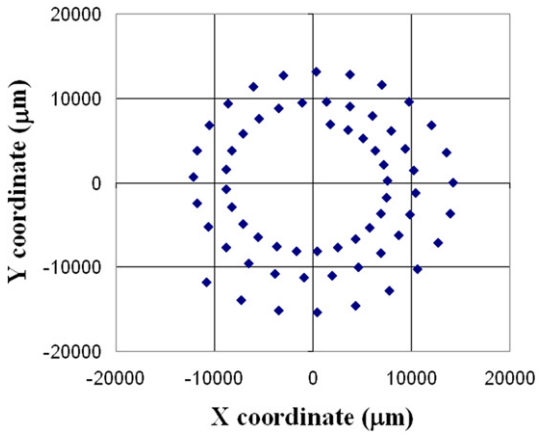


Fig. 2. Non-regular arrangement of detector locations that are used to reconstruct the 2-D interferometric images.

### 5.2. Generation, near-field corrections, and focusing of THz

The near-field correction is calculated conceptually by repositioning the detector from a planar arrangement to a spherical arrangement that matches the curvature of the incoming wavefront. The theoretical phase delay from a point source at normal incidence is subtracted from the measured phase. Our previous works [1,2] have demonstrated the need for near-field correction for detector configurations similar to Fig. 2. Here we emphasize the focusing of the reconstructed image.

Using the measured amplitudes and phases of the THz field, a near-field correction is applied to the measured phases (Eq. (7)) and correlations of all detector pairs are performed using Eq. (6). The interferometric image is reconstructed using Eq. (4). To study the depth of focus of the near-field corrected image, we reconstruct several images using a varying distance $Z_0$. This is analogous to 'focusing' the imaging array to different distances. In Fig. 3, the effect of the focusing on the reconstructed image is illustrated with reconstructed reflectivity images of a C4 plastic explosive sample. The reflectivity image (left) and the image of the same sample concealed behind a book bag (right) are obtained at 0.25 THz. For these images, the distance $Z_0$ in the image reconstruction calculation is varied between 10 and 80 cm. The actual distance between the target and the detector array is 40 cm. Note that the point image is in focus over a large range of distances, but the apparent size of the C4 depends on the focusing.

The apparent size change is partially an artifact of plotting the image as a function of lateral distance as opposed to angular extent. If the reconstructed image of Eq. (4) were plotted as function of the angular extent $(\xi, \eta)$ instead of $(x, y)$ it would be clear that the angular extent of the object does not change with focusing distance.

Other distortions in Fig. 3 are the emergence of artifacts in the background for 10 cm focusing and the emergence of side-lobe rings surrounding the point source for 80 cm focusing. In the case of $Z_o$ being less then the true distance to the point source (over focusing), too much near-field phase correction is introduced to the reconstructed image. Consequently, power in reduced in reconstructed image of the point source and transferred to structure in the background. In the case of $Z_o$ being larger than the true distance to the point source (under focusing), insufficient phase correction is introduced. The results in the growing prominence of side-lobe rings.

The under and over focusing effects become more prominent as the THz frequency is increased for a fixed arrangement of detectors. As shown in Fig. 4, as the THz frequency varies from 250, 500, to 1000 GHz, the effect of over focusing becomes more prominent. The reason is straight forward: for a fixed geometric distance of 'deforming' the locations of the detectors, the corresponding phase change increases with frequency. As the THz frequency is increased for the case of under focusing (not shown), the side-lobe rings are still present with the apparent diameter of the rings decreasing proportionally to the increasing lateral resolution as the THz frequency increases.

## 6. Interferometric image analysis

Monochromatic THz images are excellent tools in identifying metallic objects and their shape but are generally not sufficient to identify hidden explosives because of the complicating effects of barrier materials, noise, and potential image reconstruction artifacts. Terahertz imaging at multiple frequencies, however, provides two features that can be combined and exploited for accurate identification with low probability of false alarm: (i) spatial and (ii) spectral variability. Spatial analysis admits the location of object boundaries and allows shape recognition; image intensities for objects so identified can then be used to classify high or low reflectance materials. For the spectral analysis, intensity patterns from multifrequency images of an object are matched to known spectral response signatures of specific explosive agents to determine whether an agent is present. Each of the aforementioned features, spatial and spectral, can be independently employed for explosive detection. No detection method is foolproof, but the combination of the two reduces identification uncertainty and error.

In prior work, we used artificial neural networks (ANNs) [15] to analyze THz images, obtained in either reflection or transmission mode, the goal being to classify pixels or groups of pixels within the image as to their component material (e.g. explosive, barrier material, metal, skin, etc.). ANNs are collections of interconnected computational cells that simulate biological neural networks. Many ANN architectures have been proposed and have been applied successfully to identification and classification problems, mapping input patterns to outputs via nonlinear transformations. Components of the networks are adaptively and iteratively determined, often in a training stage, during which ANNs are trained to detect certain patterns by mapping known input sequences (training set) to specific outputs. In the THz interferometric imaging application, ANNs are trained to recognize the THz intensity fingerprints corresponding

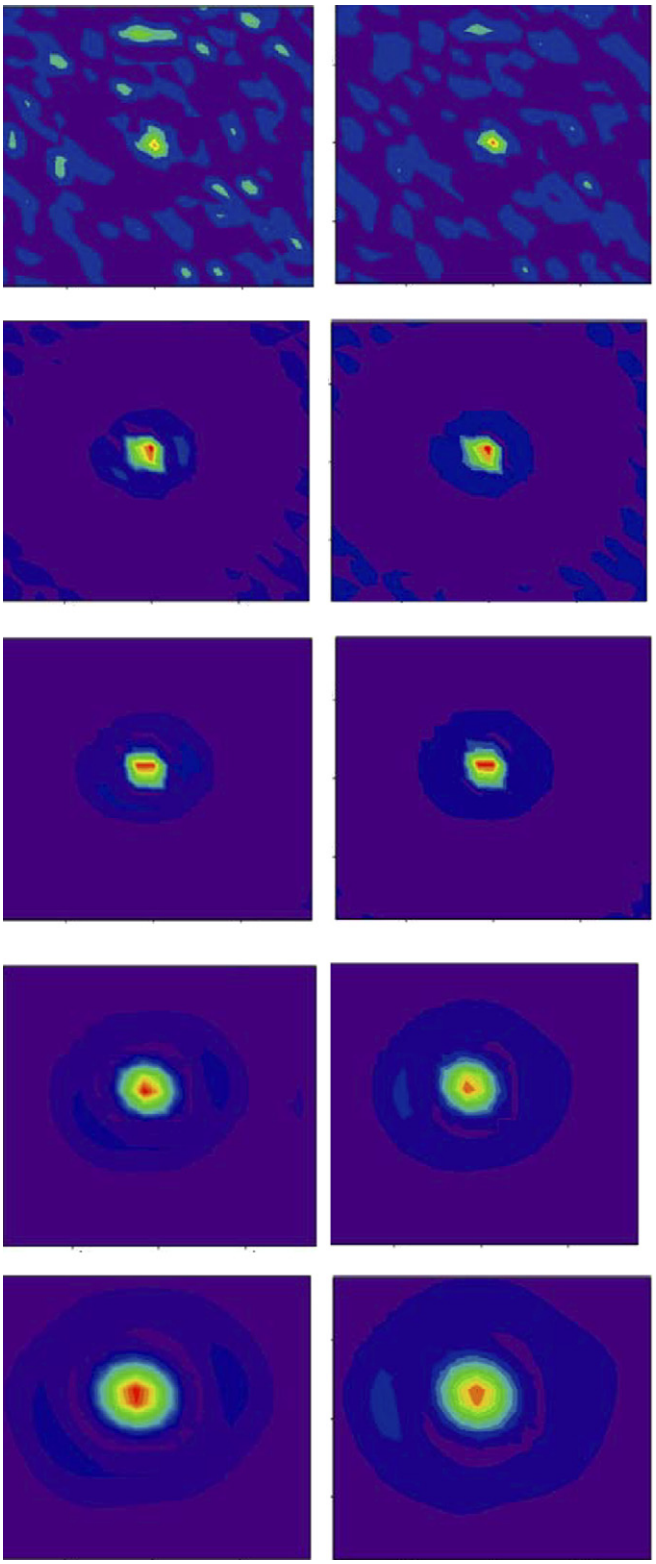

Fig. 3. Red corresponds to maximum THz intensity, while blue corresponds to minimum. Reconstructed 0.25 THz images of a C4 sample (left) and same sample concealed behind a book bag (right) as a function of focusing distance. The rows of images correspond to $Z_o = 10$, 30, 40, 60 and 80 cm, respectfully. Each image represents 20 cm by 20 cm.

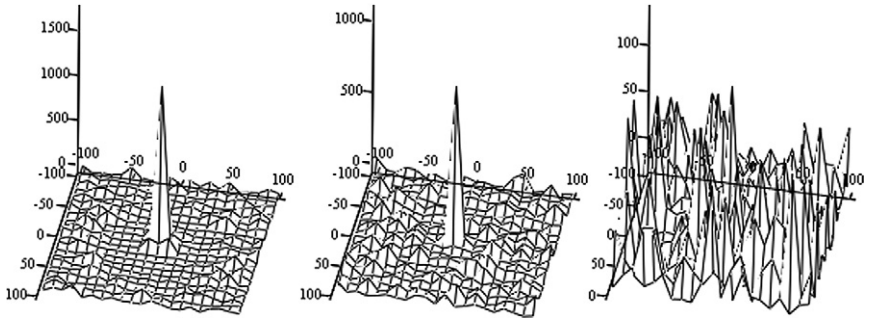

Fig. 4. Variation in the reconstructed THz image at 250, 500, and 1000 GHz. The distance to an ideal point source is 40 cm. the focusing distance $Z_o$ used in the image reconstruction is 20 cm.

to skin, fabric, explosive materials, paper, metal, etc. ANNs can be employed for classification by processing data corresponding to a single spatial point at multiple frequencies, thus exploiting only spectral variation. Alternatively, ANN inputs could consist of neighborhoods of spatially neighboring image pixels at multiple frequencies, integrating spatial and spectral analysis; using multiple neighboring pixels is expected to increase robustness in the results.

We have in the past implemented ANN architectures and applied them successfully to synthetic interferometric images for explosive identification. Multilayer Perceptrons (MLPs) [15] were applied in Refs. [16] and [2] to the analysis of a multi-frequency, reflective interferometric THz image of a suicide bomber. Images were generated at six frequencies in the THz range. Pixels (corresponding to the same location but different frequencies) were presented to an MLP, which was trained with back-propagation to match correct outputs to corresponding inputs; i.e., to identify the input patterns as metal, C4, skin, or sugar on the basis of their spectral fingerprints. Results were encouraging, especially in the detection of C4. Efforts to improve resolution led to the implementation of Radial Basis Function (RBF) networks [17], which involve a basis of analytically known functions (Gaussian waveforms in our work) in the mappings between input patterns and network outputs. Resolution was indeed improved (and was, as expected, frequency dependent).

In a similar application, MLPs were applied to synthetic reconstructed interferometric images of two objects, one metal and one consisting of C4, embedded in background. Images including the two objects were generated at frequencies of 0.7 and 0.9 THz. Reflection from the metal object was expected to be strong and flat across frequency. Reflection from C4 is frequency dependent and less intense than that from metal. This difference in imaging at different frequencies is the rule that we used for identifying materials as belonging to one or the other category (metal or C4). A third category for background was included in the analysis.

The network was trained to produce 0 at the output for background pixels. An output of 1 indicated metal and an output of 2 corresponded to C4. Training patterns consisted of sets of neighboring pixels at the two distinct frequencies; using pixel clusters instead of single elements accelerated convergence of the training stage and ensured classification results with small errors. Results were indeed excellent, correctly identifying pixels as representing metal, C4, or background, with the exception of a few cases in boundaries between different materials. Such errors can be removed in a straightforward manner by applying neighborhood restrictions to the classification results.

In Ref. [18] Kohonen Self Organizing Maps (SOMs) [19] were briefly introduced as potentially powerful tools for explosive material identification. Unlike MLPs, SOMs do not require training. Input patterns are presented to the network and are directed to regions of the output, which is typically a square grid (different output shapes can be employed as well). Weights that connect input patterns to nodes on the grid are iteratively adapted so that similar patterns are mapped to the same node or neighboring regions. Similarity is determined on the basis of a pre-selected measure, such as Euclidean distance.

Following the process of Ref. [18], we are here generating one-dimensional synthetic interferometric images including metal and C4 embedded in background at 07 and 0.9 THz. Fig. 5(a) shows the ideal images at the two frequencies; Fig. 5(b) demonstrates the reconstructed interferometric images. Two-element vectors consisting of interferometric image pixels at the same location but different frequencies were presented to a SOM with an output grid consisting of $3 \times 3$ nodes. Fig. 6 demonstrates how SOM assigns the pixels to different neighborhoods of the map. Three neighborhoods are identified at the output. The brightest one, in the region of node 7 (or, equivalently, node $(3, 1)$ of the grid) is the region where the background elements have been mapped to. The other two regions

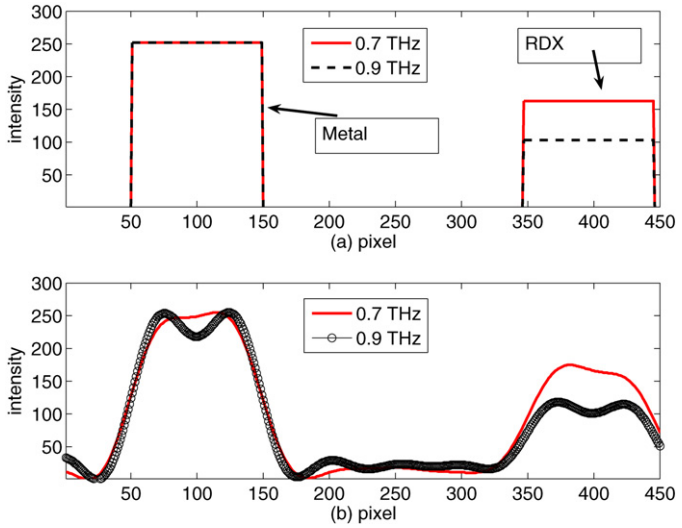


Fig. 5. Synthetic (a) ideal and (b) reconstructed one-dimensional images containing blocks of metal and RDX (C4) at two frequencies (color online).

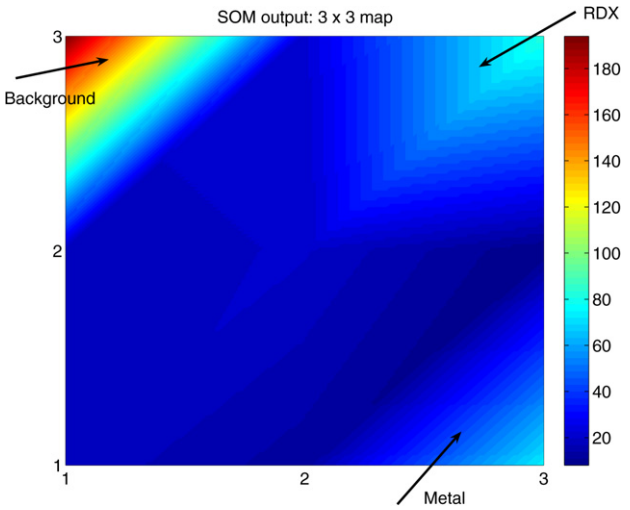


Fig. 6. Kohonen self organizing $3 \times 3$ grid: the pixels of the one-dimensional image are mapped to three clusters.

around node 3 (or $(1, 3)$) and node 9 (or $(3, 3)$) correspond to metal and C4, respectively. The background region is brighter (that is, more elements have been mapped there), because the number of background elements in the pictures is significantly larger than the numbers of C4 and metal pixels.

Fig. 7 presents the SOM results in a different form. Fig. 7(a) demonstrates the reconstructed images that were also shown in Fig. 5(b). Fig. 7(b) illustrates the SOM output node to which each pixel has been directed vs. pixel. Again we observe that metal has been mostly mapped to node 3, background to node 7, and C4 to node 9. Ambiguity is present at the boundaries of neighboring materials, as previously discussed.

The image analysis discussed so far has been performed with synthetic images. The results are promising indicating that spectral signatures can powerfully drive detection and classification of explosive materials. The question is now whether such analysis can be successfully carried out with real data. To that end, we measured reflectance of materials in the lab and used our measurements in material classification; this work was performed for a single spatial point but a range of frequencies.

Fig. 8 demonstrates spectra measured for paper, cardboard, plastic, skin, wood and plexiglass at frequencies between 0.5 and 0.9 THz. The spectrum of a sheet of aluminum foil is shown in Fig. 9; as expected, metal is a strong

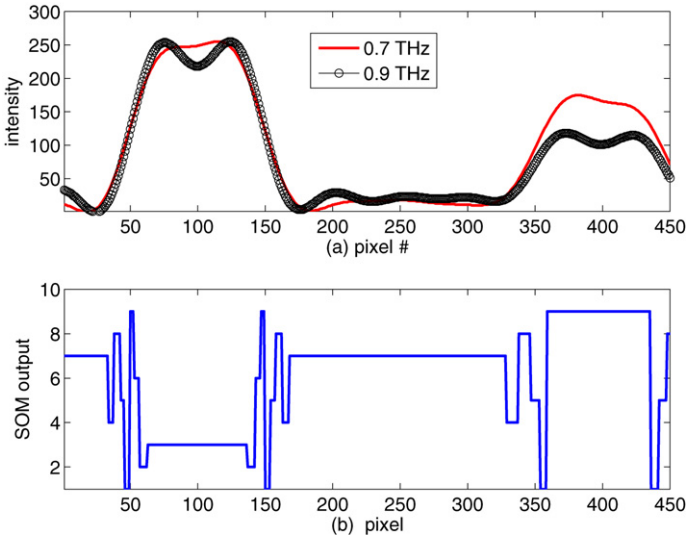


Fig. 7. (a) Reconstructed one-dimensional images containing blocks of metal and RDX (C4) at two frequencies and (b) Kohonen self organizing map output (node vs. pixel) (color online).

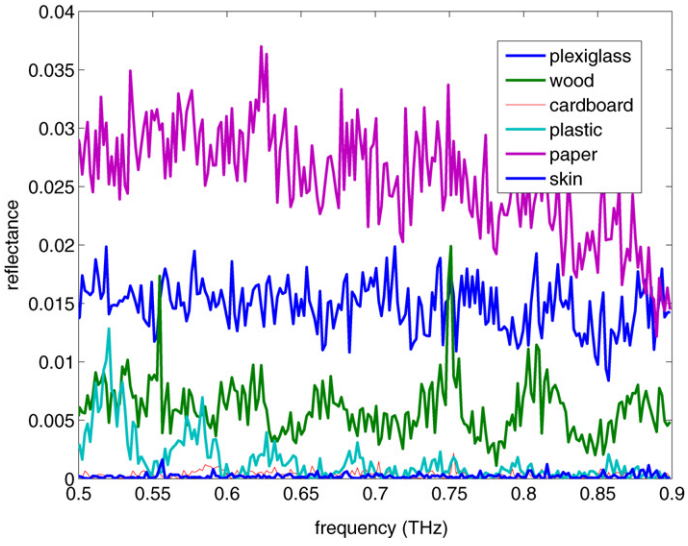


Fig. 8. Relative reflectance of paper, plexiglass, wood, plastic, cardboard, and skin (top to bottom) vs. frequency. Sharp peaks in the reflectance are experimental noise.

reflector and reflectance attains higher values for metal than for the materials of Fig. 8. Six different spectra measured from C4 are shown in Fig. 10; although the measurements indicate variations, that are likely the result of noise in the measurement process, all six C4 spectra show a very similar structure.

The thirteen spectra described above were presented as input vectors to a SOM with a $3 \times 3$ output grid. Fig. 11 illustrates the SOM output map after convergence of the iterative adaptation of the weights. All C4 spectra were mapped to node 7 (or equivalently, node $(3, 1)$ of the grid). Aluminum foil was mapped to node 1 (or $(1, 1)$). Interestingly, no other material was mapped in the neighborhood of metal (node 2 or $(1, 2)$ and node 4, or $(2, 1)$). This is because the reflectivity of aluminum foil is vastly different (higher) than that of all other considered materials, causing foil to appear dissimilar and distant (in terms of spectral response) from everything else. Skin, plastic, and cardboard, on the other hand, have similar, almost uniformly low across frequency responses as seen in Fig. 8 and are mapped to node 9

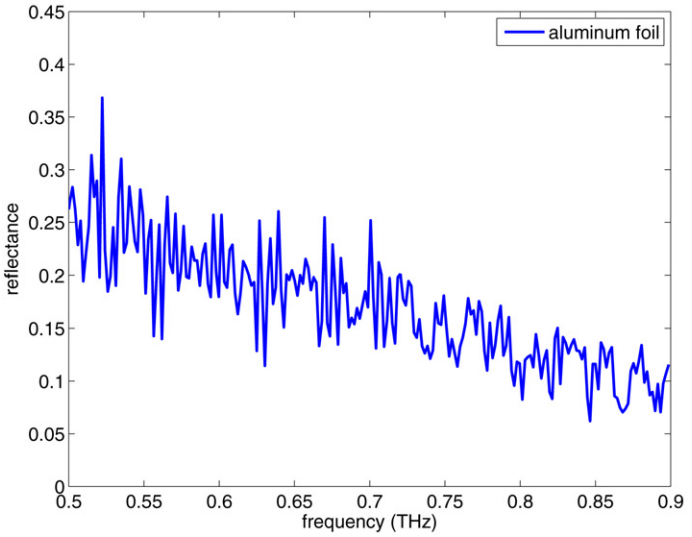


Fig. 9. Relative reflectance of aluminum foil vs. frequency (color online).

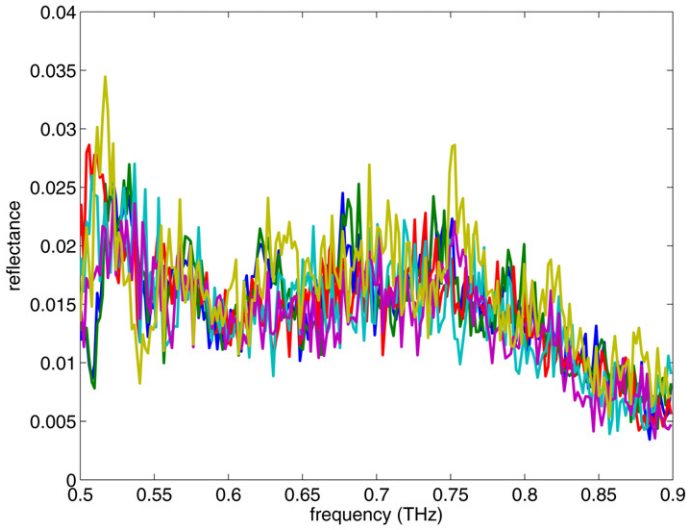


Fig. 10. Relative reflectance of C4 vs. frequency (six spectra) (color online).

(or (3, 3) of the grid). Plexiglass was mapped to node 3 (or (1, 3)), wood was mapped to node 6 (or (2, 3)), and paper was mapped to node 5 (or (2, 2)).

The SOM results from application to real data strongly support the hypothesis that reflection spectra can be successfully used as fingerprints for explosive identification. Additionally, SOMs have been demonstrated to be powerful tools in that task. Once spectra are classified using SOMs in the manner described above, spectra of newly sensed objects can be used as inputs to the network and then mapped to the region that best matches the spectral signature.

Real data results have been presented in this work for a single point classifier. Combining the above analysis with spatial information from imaging is expected to increase the robustness of the method, providing more details and reducing false classifications.

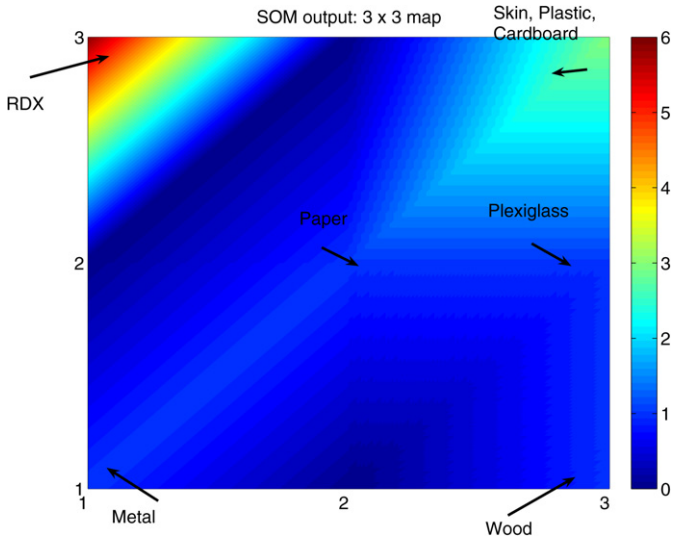


Fig. 11. Kohonen self organizing 3 × 3 grid with spectra as inputs; all C4 spectra are clearly mapped to a distinct cluster.

## 7. Conclusion

In the adaptation of Terahertz (THz) synthetic aperture imaging stand-off screening concealed weapons and explosives, the incoming THz wavefronts exhibit significant curvature. By mathematically matching the curvature of the detector array arrangement to that of the incoming THz wavefronts, the imaging array can be focused at specific distances. When the imaging array is over focused (too much phase correction), the result is a reduction in the intensity of the peak of the reconstructed image and an increase in the background intensity. If the imaging array is under focussed (too little phase correction), side-lobes appear in the image. Previously artificial neutral networks, including Multilayer perceptrons and radial basis function implementations, have been applied to the spectral analysis of the reconstructed THz image. Kohonen self-organizing maps are shown to be promising tools for differentiating the spectral signature of C4 explosive from the reflection spectra of metal and semi-transparent barrier materials.

## Acknowledgements

The authors thank the US Army for supporting our work in THz imaging. Discussions with Prof. J.M. Joseph are gratefully acknowledged.

## References

[1] J. Federici, B. Schulkin, F. Huang, D. Gary, R. Barat, F. Oliveira, D. Zimdars, THz imaging and sensing for security applications—explosives, weapons, and drugs, Semicond. Sci. Technol. 20 (1995) S266.
[2] J.F. Federici, D. Gary, R. Barat, Z.-H. Michalopoulou, Counter-Terrorism Detection Techniques of Explosives, Elsevier, 2007 (Ch. Detection of explosives by Terahertz imaging).
[3] F. Huang, B. Schulkin, H. Altan, J. Federici, D. Gary, R. Barat, D. Zimdars, M. Chen, D. Tanner, Terahertz study of 1,3,5-trinitro-s-triazine (RDX) by time domain spectroscopy and FTIR, Appl. Phys. Lett. 85 (2004) 5535.
[4] D. Zimdars, J.S. White, Terahertz reflection imaging for package and personnel inspection, Proc. SPIE 5411 (2004) 78.
[5] T. Yuan, H. Liu, J. Xu, F. Al-Douseri, Y. Hu, X. Zhang, Terahertz time-domain spectroscopy of atmosphere with different humidity, Proc. SPIE 5070 (2003) 28.
[6] E.R. Brown, Terahertz Sensing Technology, vol. 2: Emerging Scientific Applications & Novel Device Concepts, World Scientific, 2003 (Ch. Fundamentals of terrestrial millimeter-wave and THz remote sensing).
[7] D. Zimdars, J. White, G. Stuk, A. Chernovsky, G. Fichter, S.L. Williamson, Time domain terahertz detection of concealed threats in luggage and personnel, Proc. SPIE 6212 (2006) 62160O.
[8] Z. Jiang, X.-C. Zhang, Single-shot spatiotemporal terahertz field imaging, Opt. Lett. 23 (1998) 1114.
[9] A. Thompson, J. Moran, G. Swensen, Interferometry and Synthesis in Radio Astronomy, second ed., Wiley Interscience, 2001.
[10] R.A. Cheville, M.T. Reiten, R. McGowan, D.R. Grischkowsky, Sensing with Terahertz Radiation, Springer, 2003 (Ch. Applications of optically generated Terahertz pulses to time domain ranging and scattering).

[11] A. Ruffin, J. Decker, L. Sanchez-Palencia, L.L. Hors, J. Whitaker, T. Norris, J. Rudd, Time reversal and object reconstruction with single-cycle pulses, Opt. Lett. 26 (2001) 681.
[12] T.D. Dorney, J.L. Johnson, J.V. Rudd, R.G. Baraniuk, W.W. Symes, D.M. Mittleman, Terahertz reflection imaging using Kirchhoff migration, Opt. Lett. 26 (2001) 1513.
[13] J. O'Hara, D. Grischkowsky, Quasi-optic synthetic phased-array terahertz imaging, J. Opt. Soc. Am. B 21 (2004) 1178.
[14] A. Bandyopadhyay, A. Stepanov, A. Sengupta, D.E. Gary, M.D. Federici, B. Schulkin, R.B. Barat, E. Michalopoulou, D. Zimdars, J.F. Federici, Terahertz interferometric and synthetic aperture imaging, J. Opt. Soc. Amer. A 23 (2006) 1168.
[15] R.P. Lippmann, An introduction to computing with neural nets, IEEE Acoustics Speech and Signal Processing Magazine (1987) 4–22.
[16] F. Oliveira, R. Barat, B. Schulkin, F. Huang, J. Federici, D. Gary, D. Zimdars, Analysis of THz spectral images of explosives and bio-agents using trained neural networks, Proc. SPIE 5411 (2004) 45.
[17] D. Broomhead, D. Lowe, Multivariate functional interpolation and adaptive networks, Complex Systems 2 (1988) 321–355.
[18] A. Bandyopadhyay, A. Sengupta, R.B. Barat, D.E. Gary, Z. Michalopoulou, J.F. Federici, Interferometric THz imaging for detection of lethal agents using artificial neural network analysis, Int. J. Infrared Millimeter Waves 27 (2006) 1145–1158.
[19] T. Kohonen, The self organizing map, Proceedings of the IEEE 78 (1990) 1464–1480.